



## Full Text View

[Volume 29, Issue 12 \(December 1999\)](#)

### Journal of Physical Oceanography

Article: pp. 3025–3042 | [Abstract](#) | [PDF \(764K\)](#)

# Eddy Formation and Interaction in a Baroclinic Frontal Geostrophic Model

**Mateusz K. Reszka and Gordon E. Swaters**

*Applied Mathematics Institute, Department of Mathematical Sciences, University of Alberta, Edmonton, Alberta, Canada*

(Manuscript received January 29, 1998, in final form January 13, 1999)

DOI: 10.1175/1520-0485(1999)029<3025:EFAlIA>2.0.CO;2

### ABSTRACT

The authors investigate the behavior of buoyancy-driven coastal currents in a series of numerical experiments based on a two-layer frontal geostrophic model. The model focuses on baroclinic instability, allows for finite amplitude variations in the upper-layer thickness, and includes a topographic background vorticity gradient. Simulations of isolated fronts demonstrate meandering of the frontal outcropping, filamentation, and the development of both warm core and cold core eddies. Eddies can merge with each other, separate, or be reabsorbed into the current. Despite the assumption of only two layers, it is found that growth rates and length scales of the emergent features are in agreement with results of studies based on more sophisticated primitive equation models. It is determined that the cross-front topographic slope has a significant effect on the instability. In particular, a bottom that slopes in the same sense as the fluid interface hinders the growth of perturbations. Simulations with two outcroppings (i.e., coupled fronts) are also described. The authors found that such currents break up into distinct vortices that propagate very little but exhibit merging and splitting, behavior consistent with previous numerical studies involving similar models as well as laboratory experiments. Finally, an analytical nonlinear wave-packet stability theory for a marginally unstable flow with a simple linearly varying height profile is presented. The authors show that the unstable modes can saturate as solitons.

### 1. Introduction

Buoyancy-driven surface-intensified mesoscale currents play an important role in coastal dynamics, as well as ocean circulation in general. Upwelling fronts, freshwater overflows, and eastern and western boundary currents usually exhibit sharp gradients in density due to differences in temperature or salinity between water masses. Numerous examples of instability and nonlinear processes have been reported to occur off the western coast of North America (e.g., [Ikeda and Emery 1984](#); [Barth 1989a](#); [McCreary et al. 1991](#)). Many of the same mesoscale features can also be observed with respect to, for example, the much larger Gulf Stream and the much smaller Gaspé current ([Robinson 1983](#); [Benoit et al. 1985](#)). In many cases, baroclinic instability is believed to be the dominant driving mechanism in frontal evolution, especially when isopycnal deflections are not small (e.g., [Barth 1989b](#); [Ikeda et al. 1984](#); [Holland and Haidvogel 1980](#); [Mertz et al. 1988](#)). Accurate modeling of the observed variability is an integral aspect of understanding the transport of heat and salt, as well as other chemical and biological components.

To arrive at a meaningful physical description of coastal and estuarine currents, a number of models have been proposed. The use of quasigeostrophic (QG) layer models began with the work of [Phillips \(1954\)](#) and it continues to be an active area

#### Table of Contents:

- [Introduction](#)
- [Governing equations](#)
- [Numerical scheme](#)
- [Isolated front simulations](#)
- [Coupled front simulations](#)
- [Weakly nonlinear instability](#)
- [Conclusions](#)
- [REFERENCES](#)
- [APPENDIX](#)
- [FIGURES](#)

#### Options:

- [Create Reference](#)
- [Email this Article](#)
- [Add to MyArchive](#)
- [Search AMS Glossary](#)

#### Search CrossRef for:

- [Articles Citing This Article](#)

#### Search Google Scholar for:

- [Mateusz K. Reszka](#)
- [Gordon E. Swaters](#)

of research (see, e.g., [Boss et al. 1996](#)). However a small Rossby number, exhibited by many mesoscale currents, does not fully justify the application of QG theory to fronts that outcrop on the surface. The implicit assumption of small interfacial deflections (compared to the scale height) precludes the possibility of realistically modeling such fronts using QG theory. While QG estimates of initial growth rates and dominant length scales are often quite reasonable, several studies have noted that numerically integrated QG (layered as well as continuously stratified) models do not satisfactorily predict such quantities ([Ikeda et al. 1984](#); [Haidvogel et al. 1991](#)). Indeed the vertical structure of developing fronts can only be adequately described by frontal models, which do allow for outcroppings.

Barotropic frontal models include, for example, [Griffiths et al. \(1982\)](#) (hereafter referred to as GKS) and [Cushman-Roisin \(1986\)](#). In these “reduced gravity” or “1½ layer” models, variations in the upper-layer thickness are on the order of the upper-layer thickness itself. However, the lower layer is assumed infinitely deep and motionless. A number of studies indicate, though, that the dynamics of fronts can be significantly affected by the presence of a lower layer, even with a relatively large but finite thickness, which suggests that the effect of a lower layer should be accounted for (e.g., [Chassignet and Cushman-Roisin 1991](#)). There have been few studies of the baroclinic destabilization of buoyancy-driven fronts using frontal geostrophic models.

[Swaters \(1993\)](#) derived a baroclinic frontal geostrophic model, hereafter referred to as SBFM (for Swaters’s Baroclinic Frontal Model). The SBFM corresponds to a subinertial approximation of the two-layer shallow-water equations on an  $f$  plane with variable bottom topography. It focuses on baroclinic instability in the sense that in the reduced-gravity limit of the model all monotonic frontal profiles are unconditionally stable (even those with outcroppings; see [Swaters 1993](#)). The growth of the perturbations occurs due to the release of mean (frontal) potential energy through baroclinic instability, that is, through the “up” (frontal) potential vorticity gradient transport of heat associated with the lower-layer perturbations. A similar baroclinic model, scaled for a midlatitude  $\beta$  plane, was independently derived by [Cushman-Roisin et al. \(1992\)](#). While there are clear similarities between the two models, there are also differences and it is of interest to examine the full range of dynamics described in both models.

The mathematical analysis of two-layer frontal models applicable to surface-intensified currents has mostly consisted of linear stability calculations (e.g., [Killworth et al. 1984](#)), modeling individual eddies (e.g., [Cushman-Roisin and Merchant-Both 1995](#)) and tracking eddy propagation ([Chassignet and Cushman-Roisin 1991](#)). Much emphasis has been placed on the study of coupled fronts (GKS; [Paldor and Killworth 1987](#); [Paldor and Ghil 1990](#), and others). [Barth \(1989a,b\)](#) examined the linear stability of upwelling fronts, both analytically and numerically, using a two-layer shallow-water model. That study yielded several conservation statements, a stability theorem, as well as expected growth rates and length scales for growing perturbations.

The goal of this paper is to present various numerical solutions to the fully nonlinear governing equations associated with the SBFM. We show that the dynamical balances of a two-layer baroclinic frontal model can yield numerical results, qualitatively and quantitatively similar to more complex primitive equation models, for the case of isolated fronts. We will focus our discussion on the description of upwelling fronts, such as those observed off the coast of Oregon ([Barth 1989a, hereafter B89a](#)). Our results will primarily be compared with linear stability calculations of [Barth \(1989b, hereafter B89b\)](#) as well as fully nonlinear simulations by [McCreary et al. \(1991\)](#), [Haidvogel et al. \(1991\)](#), and [Samelson and Chapman \(1995\)](#); hereafter referred to as MFK, HBH, and SC, respectively. It will be shown that the SBFM captures many of the most interesting features of nonlinear frontal evolution, such as filamentation and eddy pinch-off, and gives reasonable estimates for  $e$ -folding times and dominant wavelengths.

The outline of the paper is as follows: [Section 2](#) recaps the essential ingredients in the model derivation. In [section 3](#) we provide some technical details of the numerical scheme. [Section 4](#) describes the simulations for isolated front profiles, and explores the effect of the bottom slope on frontal evolution, while the coupled front simulations are described in [section 5](#). [Section 6](#) is devoted to a weakly nonlinear theory for a marginally unstable wedgelike front in which we show that it is possible for the amplitude of the unstable modes to saturate as envelope solitons. We offer conclusions in [section 7](#).

## 2. Governing equations

Although detailed mathematical derivations of frontal geostrophic models have been fully described for a number of physical configurations, for example, [Cushman-Roisin \(1986\)](#) for a reduced gravity flow on an  $f$  plane, [Cushman-Roisin et al. \(1992\)](#) for a two-layer flow on a  $\beta$  plane, and independently by [Swaters \(1993\)](#) for a two-layer flow over sloping topography, the underlying dynamical balances assumed in the physics are sufficiently subtle that it is appropriate to review them here. Readers already familiar with the dynamical balances need only to acquaint themselves with our notation as described in our discussion of [\(2.1\)](#) and [\(2.2\)](#) below and may skip directly thereafter to the next section.

Two-layer frontal geostrophic models correspond to a subinertial asymptotic limit of the shallow-water equations in which the flow fields are geostrophic to leading order but for which ageostrophic effects are critical to determining the evolution. In the upper layer, these models allow for large amplitude variations of the upper-layer thickness so that genuine outcroppings can be described. That is, these models do not correspond to a classical QG limit in which the amplitude of the dynamic variations of the interface is small compared to the scale depth of the upper layer. The upper-layer mass equation is *fully nonlinear* and does not reduce to the statement that the flow field is solenoidal to leading order. The dynamic coupling between the two layers, which is rationally accounted for in the model derivation, is nevertheless a second-order effect. Thus, to leading order, the upper-layer dynamics is geostrophically degenerate and ageostrophic effects become dynamically important. The evolution of the upper-layer geostrophic pressure is determined at second order in the asymptotic expansion by retaining momentum advection and the dynamic coupling between the two layers within the context of a fully nonlinear upper-layer mass equation.

Since the local time rate of change of momentum terms are completely neglected in the upper layer, these models filter out

Poincaré and Kelvin waves. In addition, the neglect of these terms implies that the upper-layer dynamics will not include the local time rate of change of the relative vorticity in the resulting vorticity equation. This occurs because the timescale associated with the dynamics is longer than the advective timescale. As a consequence, the leading order ageostrophic terms in the upper-layer momentum equations do not include the time rate of change of momentum terms (but do include momentum and hence vorticity advection and the dynamical coupling between the two layers). The result is a coupled model that retains the *advection* of relative vorticity while allowing for large amplitude thickness variations in the upper layer.

The lower-layer dynamics is assumed to be QG for which the Eulerian velocity field has been scaled so as to be principally driven by the baroclinic stretching associated with the deforming interface and a background vorticity gradient, that is, the  $\beta$  effect or variable bottom topography. Because the order of magnitude of the velocity scaling in the lower layer thusly determined is smaller than that associated with the upper-layer velocity, the local time rate of change terms are the same order of magnitude as the nonlinear advective terms in the momentum equations. Hence, the vorticity equation in the lower layer will contain both advective as well as time derivative terms associated with the relative vorticity in contrast to the upper-layer vorticity equation. Additionally, of course, the lower layer is dynamically coupled back to the upper layer through baroclinic stretching. From the point of view of the lower layer, the dynamics is “weakly” nonlinear, the upper layer is “thin” compared to the scale depth of the lower layer (as is the amplitude of the dynamic deflections of the interface between the two layers), and the topography is “gently” sloping.

The SBFM can be derived from the nondimensional two-layer rigid-lid shallow-water equations written in the form

$$\begin{aligned}\sqrt{\delta}(\sqrt{\delta}\partial_t + \mathbf{u}_1 \cdot \nabla)\mathbf{u}_1 + \mathbf{e}_3 \times \mathbf{u}_1 &= -\nabla p_1, \\ \sqrt{\delta}h_t + \nabla \cdot (\mathbf{u}_1 h) &= 0, \\ \delta(\partial_t + \mathbf{u}_2 \cdot \nabla)\mathbf{u}_2 + \mathbf{e}_3 \times \mathbf{u}_2 &= -\nabla p_2, \\ \nabla \cdot \mathbf{u}_2 &= \delta\{h_t + \nabla \cdot [u_2(h + h_B)]\}, \\ p_1 &= h + \sqrt{\delta}p_2,\end{aligned}$$

where the subscripts 1 and 2 denote, respectively, upper- and lower-layer quantities with  $\mathbf{u}_{1,2}$ ,  $p_{1,2}$ ,  $h$ , and  $h_B$  the velocities, dynamic pressures, upper-layer thickness, and bottom topography, respectively, and where

$$\delta = \frac{h_*}{H}$$

is the ratio of the upper-layer scale thickness ( $h_*$ ) to the lower-layer scale thickness ( $H$ ).

Written in this form the key asymptotic parameter is  $\delta$  for which we assume  $0 < \delta \ll 1$ . The subinertial time scale is given by  $(f\delta)^{-1}$  and the length scale is given by

$$L = \frac{\sqrt{g'h_*}/\sqrt{\delta}}{f},$$

where  $f$  and  $g'$  are the Coriolis parameter and reduced gravity, respectively. The length scale is intermediate between the internal deformation radius associated with each individual layer since, assuming  $\delta$  is small,

$$\frac{\sqrt{g'h_*}}{f} \ll \frac{\sqrt{g'h_*}}{\delta^{1/4}f} = L = \frac{\delta^{1/4}\sqrt{g'H}}{f} \ll \frac{\sqrt{g'H}}{f}.$$

If we think of the lower-layer deformation radius as a “basin” length scale, the SBFM can be thought of as an intermediate length scale model, in the sense of [Charney and Flierl \(1981\)](#), in which the dominant nonlinearity arises not due to the advective terms in the momentum equations but rather due to density or thickness gradients in the mass or continuity equation. The scalings for the upper and lower layer velocities are given by, respectively,  $(\delta)^{1/2}fL$  and  $\delta fL$  and the dynamic pressures are scaled geostrophically. The upper-layer velocity scaling is larger than the scaling for the lower-layer velocity and this results in the upper-layer advective terms in the momentum equations being an order of magnitude larger than those in the lower-layer momentum equations.

The model equations are derived by introducing a straightforward asymptotic expansion in powers of  $(\delta)^{1/2}$  into the above shallow-water equations, the details of which we do not describe here (see [Swaters 1993](#)). If the leading order upper-layer frontal thickness is denoted by  $h(x, y, t)$ , which is also the leading-order geostrophic pressure in the upper layer, and the leading-order lower-layer geostrophic pressure is denoted by  $p(x, y, t)$ , the SBFM can be written in the form

$$(\Delta p + h)_t + J(p, \Delta p + h + h_B) = 0, \quad (2.2)$$

where the notation is standard (see [Fig. 1](#)) with the horizontal coordinates given by  $(x, y)$ ,  $t$  is time, and  $J(A, B) = A_x B_y - A_y B_x$  with alphabetical subscripts denoting partial differentiation (unless otherwise indicated). For details of the derivation, as well as a description of the underlying noncanonical Hamiltonian structure and the linear and nonlinear stability theory, see [Swaters \(1993\)](#) and [Karsten and Swaters \(1996\)](#). Boundary and initial conditions appropriate for our numerical work will be described in the following section.

It is also worth pointing out that (2.1) and (2.2) correspond to the (nontrivial) leading-order potential vorticity (PV) equations in each layer, respectively, in which the potential vorticity in the lower layer is given by  $\Delta p + h + h_B$  and in the upper layer it is given by  $1/h$ . Alternatively, (2.1) can be thought of as the leading-order mass conservation equation for the frontal layer in which the velocity field is determined by the leading-order ageostrophic terms that arise from the upper-layer momentum equations. The inclusion of these terms leads to a model that is cubically nonlinear with respect to  $h$  [see (2.1)]. These terms correspond to the advection of frontal vorticity by the frontal flow and are necessary for instability. The reason why these advective terms are cubically nonlinear, compared to quadratically nonlinear as in QG theory, is a result of the fact that the underlying scalings used to derive (2.1) assume that, even at leading order, the upper-layer continuity equation is fully nonlinear as a consequence of allowing for finite amplitude thickness variations. The higher-order nonlinearity is a direct consequence of developing a model which can, in principle, describe the formation and evolution of outcroppings.

However, the presence of these horizontal (frontal) shear terms is not *sufficient* to generate instability in the model, and it is not necessary for there to be an inflection point in the frontal velocity profile. As shown by [Swaters \(1993\)](#) (see also [Karsten and Swaters 1996](#)), there is *no instability possible* in the reduced-gravity limit corresponding to setting  $p = 0$  in (2.1) and ignoring (2.2) (which is the model derived by [Cushman-Roisin 1986](#)), for any monotonic frontal profile, for example, an upwelling front. The presence of the second layer, that is, the baroclinic coupling, is necessary for instability. This point is important because the instabilities (and the subsequent eddy dynamics) we describe here do not correspond to simply baroclinically modified barotropic instabilities of the sort described, for example, by [Killworth and Stern \(1982\)](#), [Killworth \(1983\)](#), or [Paldor \(1983\)](#), among many others, but are explicitly baroclinic in development.

### 3. Numerical scheme

[Equations \(2.1\)](#) and [\(2.2\)](#) were numerically solved as the system:

$$h_t = J\left(h, p + h\Delta h + \frac{1}{2}\nabla h \cdot \nabla h\right), \quad (3.1)$$

$$q_t = J(q, p), \quad (3.2)$$

$$\Delta p = q - h - h_B, \quad (3.3)$$

where we have introduced the lower-layer potential vorticity,  $q = \Delta p + h + h_B$ .

We chose to use an explicit, finite-difference algorithm, which is leapfrog in time and central in space (second-order accurate in both cases). The Jacobian terms are approximated via the [Arakawa \(1966\)](#) formula, which preserves energy and enstrophy conservation and the underlying skew-symmetry. A conjugate-gradient technique is used to invert the Laplacian in (3.3) to recover the lower-layer pressure at each time step. We introduced the Robert filter ([Asselin 1972](#)) to help suppress the computational mode. Numerical friction proportional to  $\Delta^8 h$ , with a coefficient of  $5.0 \times 10^{-20}$ , is employed in the upper-layer [equation \(3.1\)](#) to eliminate small-scale noise.

The computational domain is a periodic channel given by

$$\Omega = \{(x, y) | 0 < x < x_{\max}, 0 < y < L\}. \quad (3.4)$$

All flow fields are assumed to be smoothly periodic across  $x = 0, x_{\max}$  and a no-normal-flow condition is applied on the channel walls at  $y = 0, L$ . That is, we employ Dirichlet boundary conditions on both geostrophic pressures,  $p$  and  $h$ , such that

$$\left. \frac{\partial h}{\partial x} \right|_{0,L} = \left. \frac{\partial p}{\partial x} \right|_{0,L} = 0.$$


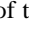
To focus on the baroclinic problem, initially there is no *mean* flow in the lower layer. Since our choice of initial conditions has  $p = 0$  on  $y = 0, L$  at  $t = 0$ , the boundary values of the  $p$  are zero for all  $t$ . The boundary values of  $h$  remain fixed at their initial  $x$ -invariant values, as determined by the initial profile. We did a number of experiments before deciding on the width of the channel. The channel width is typically chosen so that the channel walls do not significantly affect frontal instabilities or eddy interactions.

Tracking of the interfacial outcropping can be problematic in numerical simulations. As shown in a detailed asymptotic analysis by [Swaters \[1993, see sec. 2b Eqs. \(2.20\) and \(2.21\)\]](#), however, in the frontal geostrophic limit associated with the SBFM, the appropriate kinematic and dynamic boundary conditions on an outcropping reduce to [\(2.1\)](#) itself when *evaluated on the outcropping*, regardless of whether or not  $h$  smoothly vanishes. Since the upper-layer [equation \(2.1\)](#) is trivially satisfied whenever  $h = 0$ , the location of the outcropping is determined automatically by simply integrating [\(2.1\)](#) over the entire domain. This is a clear advantage of the SBFM, which underscores its utility in numerical process studies related to the dynamics of outcroppings compared to, for example, primitive equation simulations.

For all the numerical simulations we describe here, the initial condition for the upper layer was simply the undisturbed frontal profile. The destabilization by introducing, as an initial condition, a band limited superposition of waves of various wavelengths that satisfied the periodicity and boundary conditions with random phase shifts and amplitudes into the lower layer. The initial value of the lower-layer perturbation kinetic energy was 10% of the upper-layer kinetic energy; that is,

$$\frac{\iint_{\Omega} \nabla p_0 \cdot \nabla p_0 \, dx \, dy}{\iint_{\Omega} h_0 \nabla h_0 \cdot \nabla h_0 \, dx \, dy} = 0.1, \quad (3.5)$$

where  $p_0(x, y) = p(x, y, 0)$  and  $h_0(y) = h(x, y, 0)$ . As the leapfrog scheme requires initial data at the first two time steps and the qualitative details of the initial perturbation are not particularly important in the instability simulations, we prescribed the same initial data at  $t = 0$  and  $t = \Delta t$ .

We will examine the destabilization of two types of frontal profiles, corresponding to an isolated front ([Fig. 2a](#) ) and a coupled front ([Fig. 2b](#) ) , respectively. The initial form for the nondimensional upper-layer thickness for each of these simulations is given by, respectively,

$$h_0 = \begin{cases} 0, & y \leq Y_1 \\ \frac{1}{2} \left\{ 1 + \sin \left[ \pi \left( y - \frac{Y_1 + Y_2}{2} \right) / (Y_2 - Y_1) \right] \right\}, & y \in (Y_1, Y_2) \\ 1, & y \geq Y_2, \end{cases} \quad (3.6)$$

and

$$h_0 = \max \left\{ \exp \left[ -a^2 \left( y - \frac{L}{2} \right)^2 \right] - b, 0 \right\}, \quad (3.7)$$

where  $Y_1 < Y_2$ ,  $a$  and  $b$  are appropriate constants. The (positive) constant,  $b$ , provides an outcropping on each side of the current axis and allows us to choose the actual current width.

It is worth noting that the exact shape of each of the above profiles has no significant effect on the behavior of the front. More important are features such as frontal height, general width of the current, and the maximum slope of the front.

#### 4. Isolated front simulations

##### a. Description of results

Many numerical studies have been aimed at modeling the nonlinear instability processes arising in mesoscale currents. MFK developed a 2½-layer shallow water model to examine the dynamics of the circulation near an eastern ocean boundary. HBH modeled filament formation in the California Current System, using a semispectral isopycnic primitive equation model. For fronts in the North Atlantic Subtropical Convergence Zone, SC used the model introduced by HBH but focused on the development of cyclonic eddies early in the evolution of the front. We emphasize that direct comparisons between the present work and the above studies should be made with caution due to differences in assumed scales of motion as well as other fluid properties. Nevertheless, the physical phenomena under consideration are similar enough that some quantitative comparisons can be instructive. We remind the reader that the initial conditions for  $h$  and  $p$  have been described in [section 3](#).

We performed a number of experiments with the SBFM, having initialized the upper layer as the isolated front given by

(3.6) with  $Y_1 = 3.0$  and  $Y_2 = 5.0$ . As a simple approximation of typical bathymetry in coastal regions, bottom topography was defined (nondimensionally) by

$$h_B = \max \left[ \frac{1}{2} (1 + \cos(\pi y/6)), 0 \right]. \quad (4.1)$$

The scale of this  $x$ -invariant topography is on the order of the upper-layer thickness, and its location is such that the early frontal evolution is not affected (but meanders closer to the coast may be affected later). Following B89a, we employ the following parameter values, consistent with upwelling fronts observed off the Oregon coast:  $R = 7$  km,  $\bar{h} = 50$  m,  $\delta = 0.25$ , and  $\bar{L} = 10$  km, where  $R$  is the baroclinic Rossby radius,  $\bar{h}$  is the scale of upper-layer thickness,  $\delta$  is the ratio of upper-layer thickness to total fluid depth, and  $\bar{L}$  is the length scale predicted by the model. Accordingly, our channel was 250 km long and 150 km wide, and the frontal region occupied a distance of approximately 30 km in the cross-channel direction. The domain was discretized into a  $250 \times 150$  grid, with each grid element approximately 1 km on a side. A time series of this simulation is shown in Fig. 3, at 0, 9, 15, and 18 days. Each frame in the series is a contour plot of the upper-layer thickness  $h$ , and the contour interval is 12.5 m. Regions where  $h$  vanishes are shaded.

Initially the jet has no  $x$  variation (Fig. 3a) and its maximum geostrophic velocity is  $-0.25$  m s<sup>-1</sup>. The outcropping deforms into a series of waves (Fig. 3b) as the instability feeds on the available potential energy stored in the sloping interface. We emphasize that only the baroclinic mechanism is operative here since for monotonic fronts no instability is possible in the barotropic limit of the model (Swaters 1993). The length scale associated with the fastest growing mode in our simulations was always larger than the Rossby radius for the upper layer, which suggests an efficient release of potential energy (Pedlosky 1987). We estimate an average alongfront wavelength of 63 km and an  $e$ -folding timescale of 7 days. In comparison, observations off the Oregon coast, as described in B89b, suggest length scales of 32–60 km and  $e$ -folding times of 2–4 days. The linear model in that same study seems to predict a wavelength of 49 km and an  $e$ -folding time of 2.2 days, for the parameter values we have chosen. MFK report length scales of about 42 km for the early phase of the destabilization. The comparison with SC is less straightforward since their model was continuously stratified. However the fastest growing mode in their simulations had a wavelength of 71 km and the  $e$ -folding time appeared to be 2.3 days. Clearly, the growth rate of the instability in our simulations is smaller than those of B89b and SC, though not unreasonably so. The discrepancy is likely due to the fact that we only consider baroclinic instability, while the other two models allow both barotropic and baroclinic mechanisms to work concurrently. Nevertheless, the length scales predicted by the SBFM are very reasonable.

Tracking the disturbances throughout the first few days of the experiment, we determined a downstream phase speed of  $5$  cm s<sup>-1</sup>. This is slower than the speeds observed off the coast of Oregon (8–14 cm s<sup>-1</sup>) but faster than the predicted theoretical velocity in B89b (1–2 cm s<sup>-1</sup>). It is very close, however, to the downstream velocity of  $7$  cm s<sup>-1</sup> reported by MFK in their simulations. Neither HBH nor SC comment on the propagation of the initial disturbances.

By day 15 of the simulation several warm and cold filaments have developed (Fig. 3c). This is very reminiscent of intrusions seen in the simulations of HBH as well as MFK. Cold filaments associated with the California Current can penetrate hundreds of kilometers in the cross-shelf direction, transporting nutrients into the deep ocean. Filaments in our simulations were 25–50 km wide, in close agreement with observations (see, e.g., Kosro 1987). Warm filaments, composed of upper-layer fluid, were at most 50 m deep, while cold filaments naturally spanned the entire fluid column. They rarely penetrated across the whole width of the channel (150 km). Similar “fingers” were seen in the numerical simulations of MFK. Understandably, the filaments reported by HBH had greater spatial extent since their model incorporated larger horizontal and vertical scales a priori. While the growth of fingerlike projections in our experiments was not as pronounced or prolonged as in those of HBH, it should be noted that unlike HBH, the present study utilized an  $x$ -invariant coastline and bottom topography.

At day 18 (Fig. 3d) the front has evolved quite considerably, with two isolated warm core eddies and one large cold core eddy clearly visible. Eddies that we have observed are elliptical in shape and typically have a diameter of 40–60 km (comparable to the initial width of the current itself). Satellite images and drifter data from the Coastal Ocean Dynamics Experiment suggest eddy diameters of 45 to 65 km (Kosro 1987) in the coastal waters of northern California. MFK reported cyclonic and anticyclonic eddies with diameters ranging from 50 to 75 km in their numerical study. From the SBFM simulations, we conclude that eddies which do not merge with each other and escape reabsorption by the coastal circulation tend to propagate parallel to the shore in the positive  $x$  direction (i.e., upstream). It must be emphasized, that these are true, distinct eddies whose isopycnals intersect the surface, rather than simply warm or cold anomalies in the upper layer. We should also note the intensification of velocities in the main frontal region. Figure 4 is a plot of the upper-layer geostrophic velocities at day 18 (i.e., corresponding to Fig. 3d). The current has become rather narrow, and is concentrated near the main frontal outcropping. Local surface velocities of approximately  $1$  m s<sup>-1</sup> can be seen in association with some meanders and isolated vortices. Similar velocities were observed by HBH.

Much information can be gained about the vertical structure of these features by examining the upper and lower layer flow fields together. Figure 5 shows two contour plots of the (nondimensional) lower-layer pressure at (a) day 9 and (b) day 18, that is, corresponding to Figs. 3b and 3d, respectively. The contour interval is 0.15 in (a) and 0.4 in (b), with negative pressure values marked by dashed contours. In (a) the  $p$  field has organized itself into a wave train localized beneath the upper-layer current. Each of the low pressure cells in the lower layer can be associated with an adjacent meander (high pressure areas) in the upper layer. The cyclonic vorticity in the ambient fluid (Fig. 5a) tends to advect the wave crests of the current, thus leading to the familiar “backward breaking” behavior (Fig. 3b) seen in laboratory experiments of

Griffiths and Linden (1981) and Griffiths and Linden (1982). This pairing of upper-layer and lower-layer vortical cells is similar to the development of eddy dipoles reported by MFK, HBH, and others. [Figure 5b](#) shows a collection of large scale vortical structures in the lower-layer streamfunction. High pressure cells correspond to positive anomalies in the upper-layer thickness, such as meanders and eddies. Over a long time, the lower layer favors large length scales, and smaller anomalies are smoothed out, although this tendency may be an artefact of inverting the Laplacian in [\(3.3\)](#).

### *b. Effect of bottom slope*

The velocities of surface currents often become intensified near coastlines where the ocean is typically very shallow, and this is when the ocean bottom plays an important role. Since in this discussion we are mainly interested in the qualitative aspects of the correlation between bottom slope and perturbation growth rate, we will deal with nondimensional quantities only. In order to minimize the number of potential parameters in our investigation, we employed a simple, linearly sloping bottom; that is,

$$h_B = -sy, (4.2)$$

where positive  $s$  indicates a bottom sloping downward in the offshore direction. A series of simulations was performed, varying the bottom slope  $s$  from  $-2.0$  to  $2.0$  at intervals of  $0.25$ . Because there is no initial mean flow in the lower layer, the lower-layer kinetic energy (KE) is a good indicator of the overall growth of the perturbation. We calculated the growth rate of the lower-layer KE for the linear instability stage in each simulation, and plot the results versus  $s$  in [Fig. 6](#).

As  $s$  decreases, the growth rate increases. The curve is not monotonic because, as  $s$  changes, the effective depth of the lower layer underneath the front also changes. This in turn affects the wavenumber of the fastest growing mode. Thus, at  $s \approx -1$  we see a transition from a wavenumber 2 instability to a wavenumber 3 instability. The important point, however, is that whenever the bottom slopes in the opposite sense to the fluid interface, growth is enhanced, and the effect is stronger as the topography becomes steeper. A similar result was found for the two-layer QG channel model by [Mechoso and Sinton \(1981\)](#).

If  $s$  is positive (i.e., bottom slopes in the same sense as the interface) and small, the instability still grows but at a much lower rate. Again, this is consistent with the findings of [Mechoso and Sinton \(1981\)](#), as well as B89b who used a primitive equation model. For  $s > 1$  no growth is observed. Since the maximum nondimensional interfacial slope in these simulations was approximately 1, this result is in agreement with the stability condition

$$0 < \max_y \left\{ \frac{\partial h_0}{\partial y} \right\} < s. \quad (4.3)$$

The above criterion for the SBFM can be obtained as part of the linear instability calculation ([Swaters 1993](#)). It is well known in QG theory that strong bottom topography (or indeed the  $\beta$  effect) has the potential to completely stabilize a front (see, e.g., [Pedlosky 1987](#)). It should also be noted that, like the Phillips model, the SBFM does not require that the cross-shelf potential vorticity gradient vanishes for instability. For example, if the PV gradients in each layer are of opposite sign, growth of normal mode perturbations is possible.

In an actual oceanographic setting the effect of the bottom slope is probably less pronounced since the front is cushioned from the influence of topography by stratification in the ambient fluid. The tendency of homogeneous models to overestimate the importance of bathymetry in the vorticity balance may be rectified by an appropriate rescaling of the topography. Finding a scaling parameter suitable for mesoscale models could be a worthwhile future investigation. Nevertheless, we believe that these findings do give insight into the behavior of real ocean systems. It is interesting to observe, for example, that the Gulf Stream sheds most of its warm core and cold core eddies after it leaves the continental shelf. That is, vigorous instability is seen only after the influence of the downward slope is no longer present ([Bush et al. 1995](#)).

The process of eddy pinch-off, as described in the previous section, undoubtedly involves barotropic shear. While the growth of meanders and filaments in the present model is strictly a baroclinic effect, once such a meander or filament is formed, opposing velocities on either side surely enhance the separation. We have found that the qualitative aspects of this behavior are similar, no matter what the bottom slope (except when the bottom slope exceeds the maximum interfacial slope, as in [Fig. 6](#)). These considerations naturally lead us to the discussion of coupled fronts, as in the following section.

## **5. Coupled front simulations**

### *a. Description of results*

A current sometimes exhibits two outcroppings of one density surface, forming a “filament” (e.g., [Gill 1982](#); [Mertz et al. 1990](#)). There are also ample data involving these surface “coupled fronts” from laboratory experiments, most notably GKS. The GKS study presented an asymptotic theory in the reduced-gravity regime, which seems to predict the correct length scales and structure of the instability, at least for narrow currents (as compared with the deformation radius). They also noted that the exact form of the PV profile is not a critical factor in the instability mechanism. [Pavia \(1992\)](#) performed several numerical experiments using a Lagrangian “particle in cell” method to model filament evolution. He used a one-layer primitive equation model, as well as the frontal geostrophic model of [Cushman-Roisin \(1986\)](#). In both cases he observed the development of a series of elliptical eddies, quite similar to the instability reported by GKS.

Here we present a numerical simulation with the upper-layer thickness initialized as the coupled profile (3.7) with  $a = 1.5$  and  $b = 0.2$ . This forms a current about two units across, or 20% of the channel width. Parabolic and piecewise-linear coupled fronts, which we also tested, yielded qualitatively similar evolution. As in the isolated front simulations in the previous section, a random perturbation was introduced into the lower-layer pressure field to induce an instability in the flow. Since the form and dominant length scale of the instability can easily be compared with the initial current, we have not imposed any particular scaling on the variables, leaving them in nondimensional form. The important point is that the initial current half-width must be smaller than the Rossby radius for the flow. For wider currents, each front tends to become unstable independently (GKS), in which case the isolated front simulations of section 4 would be more applicable. Again, we remind the reader that the initial conditions for  $h$  and  $p$  have been described in section 3.

A typical simulation can be summarized as follows. The current deforms asymmetrically and promptly breaks up into distinct eddies, whose size is comparable to the width of the current, in accordance with GKS. The eddies are elliptical, but with small eccentricity. They rotate clockwise, that is, anticyclonically, where we mean that there is an overall rotation of the ellipse about its center. This was also observed by Pavia (1992). While the slope of the bottom topography seems to have little impact on the initial breakup of the current, here we chose  $s = 0.5$ , as we found that a sloped bottom is conducive to eddy–eddy interactions later in the simulation. Figures 7a–e show five frames from the evolution of a frontal filament, at nondimensional times  $t = 0, 2, 5, 8,$  and  $13$ . Here the domain was 12 units in the along-channel direction and 10 in the cross-channel direction with  $\Delta x = \Delta y = 0.1$ . The upper-layer streamfunction values range between 0 and 0.8 and the contour intervals are 0.2 in all five plots. Again, shaded regions correspond to  $h = 0$ , that is, the water column is composed entirely of lower-layer fluid.

Figure 7a is the initial configuration, where the current is approximately two units wide. If we choose the typical (GKS) parameter values  $\bar{h} = 5$  cm,  $g' = 5$  cm s<sup>-2</sup>,  $f = 1.1$  s<sup>-1</sup>,  $\delta = 0.17$ , then the Rossby radius is approximately 4.5 cm and our length scaling is 7 cm. Consequently, the dimensional current half-width is 7 cm, certainly less than twice the Rossby radius. Perturbations develop along both fronts, and the current begins to break up in Fig. 7b. Here the instability is mainly due to a coupling of streamlines, a mechanism markedly different from the one associated with much wider currents and isolated fronts (GKS). GKS proposed that narrow filaments tend to be dominated by barotropic instability, while baroclinic instability plays an important role when the streamlines are far apart. Indeed, both models used by Pavia (1992) were barotropic.

The eddies are fully formed and separated in Fig. 7c. Adopting the aforementioned depth ratio, it is possible to estimate the timescale of this process. Based on several such simulations, we can safely say that eddies are formed within 5 to 10 rotation periods, which agrees with both the laboratory experiments of GKS as well as the numerical study of Pavia (1992). It should be noted however, that the shape of the eddies resembles those in GKS much more than the nearly circular eddies obtained from the analogous reduced-gravity frontal model (Pavia 1992). The average ratio of minor axis to major axis for the eddies in Fig. 7c is approximately 0.7, which agrees more favorably with the one-layer primitive equation model (Pavia 1992). We refer the reader to Cushman-Roisin and Merchant-Both (1995) for a thorough examination of isolated eddies in a two-layer ocean.

Once formed, vortices in our simulations tend to be located just off the current axis and do not usually propagate in any direction. Their locations and translation can be influenced by a sloping bottom through strong anomalies in the lower-layer pressure. However this effect is transitory and yields no consistently preferred direction of motion as would be the case on a  $\beta$  plane. With a flat bottom, the arrangement of the eddies seems to be dictated by conservation of total momentum, which is zero for the initial current. We have observed that the emergent vortices are quite stable when isolated but, if any two come close to one another, they are likely to merge. The resulting oblong body does not appear to be stable and can easily split into two separate eddies again. A merger can be seen in Fig. 7d and a subsequent splitting in Fig. 7e. Similar behavior was reported by Pavia (1992). The number of vortices produced is heavily influenced by the length of the channel domain. It should also be noted that the eddy development in a shear flow is more rapid than in the isolated front simulations described above. Undoubtedly, the shear present in the basic flow is a source of energy, which hastens the instability process.

## 6. Weakly nonlinear instability theory

The above results clearly indicate the development and growth of unstable waves, and subsequent saturation of the instability due to nonlinear processes. To gain a better understanding of these dynamics, we present a weakly nonlinear analysis for a marginally unstable mode of a steady wedgelike frontal profile. Although a wedge profile without isopycnal outcroppings is rather idealized, it does allow us to study available potential energy release and nonlinear interactions, that may saturate the growth of instabilities. Griffiths and Linden (1981) were confident that their theory, which made use of such a profile, explained many of the instability characteristics observed in their laboratory experiments. The derivation of an amplitude equation for even this simple front is rather involved, but the procedure itself is a standard one, and here we follow Pedlosky (1987). More in-depth studies may be found in a series of papers by Pedlosky (1970, 1972, 1982, 1983). As we shall show, marginally unstable modes can saturate as envelope solitons. Although the model is valid for general bottom topography, we will focus on the linearly sloping bottom given by

$$h_B = -sy. \quad (6.1)$$

This bottom topography, while very simple, nevertheless facilitates the interpretation of the role of a background potential vorticity gradient.

We consider an upper-layer wedge profile of the form



$$n_0 = 1 + \alpha \left( y - \frac{1}{2} \right), \quad (6.2)$$

where  $\alpha$  is the (constant) slope of the fluid interface. For a discussion of the general linear instability problem for this model we refer the reader to [Swaters \(1993\)](#). Substituting (6.2) into the linear instability problem associated with (2.1) and (2.2), we must assume that  $\alpha$  and  $s$  are small in order to obtain analytical solutions (for full details, see [Reszka 1997](#)). Accordingly, it is convenient to rescale  $\alpha$  and  $t$  via

$$\alpha = s\tilde{\alpha} \quad \text{and} \quad t = \tilde{t}/s, \quad (6.3)$$

and immediately drop the tildes.

Assuming normal-mode perturbation solutions:

$$(p, h) = (\tilde{p}, \tilde{h}) \exp[ik(x - ct)] + \text{c.c.}, \quad (6.4)$$

(where c.c. refers to the complex conjugate of the preceding term), the linear instability problem reduces to

$$h'' - \left( \frac{c}{\alpha} + k^2 \right) h + \tilde{p} = 0, \quad (6.5)$$

$$\tilde{p}'' - \left( \frac{\alpha - 1}{c} + k^2 \right) \tilde{p} + h = 0, \quad (6.6)$$

where  $k$  is the along-channel wavenumber,  $c$  is the (complex) phase speed, and the primes refer to derivatives with respect to  $y$ . The no-normal-flow boundary condition on the channel walls implies, for arbitrary  $k$ ,

$$\tilde{p}(0) = \tilde{p}(L) = \tilde{h}(0) = \tilde{h}(L) = 0. \quad (6.7)$$

The solutions are

$$(\tilde{p}, \tilde{h})(y) = (A, B) \sin(l y), \quad (6.8)$$

where  $A$  and  $B$  are constants and  $l$ , the quantized cross-channel wavenumber, is given by  $l = n\pi/L$ ,  $n \in \{1, 2, 3, \dots\}$ . We now have the general form of the normal-mode perturbation solutions, that is,

$$(p, h)(x, y, t) = (A, B) \sin(l y) \exp[ik(x - ct)] + \text{c.c.} \quad (6.9)$$

Using these solutions, we can write (6.5) and (6.6) in matrix form,

$$\begin{bmatrix} K^2 + \frac{\alpha - 1}{c} & -1 \\ -1 & K^2 + \frac{c}{\alpha} \end{bmatrix} \begin{bmatrix} A \\ B \end{bmatrix} = \begin{bmatrix} 0 \\ 0 \end{bmatrix}, \quad (6.10)$$

where  $K^2 = k^2 + l^2$  is the *total wavenumber* squared. For the problem to allow nontrivial solutions we require that the determinant of the coefficient matrix is identically zero; that is,

$$(cK^2 + \alpha - 1)(\alpha K^2 + c) - ac = 0, \quad (6.11)$$

which yields the following *dispersion relation*

$$c = \frac{1 - \alpha K^4 \pm [(\alpha K^4 - 1)^2 - 4\alpha(\alpha - 1)K^4]^{1/2}}{2K^2}. \quad (6.12)$$

The marginal stability boundary is obtained by setting the discriminant in (6.12) equal to zero. There are two curves of marginal stability (MSC; see [Reszka 1997](#)), hereafter referred to as the upper and lower branches, respectively (see [Fig. 8](#)). We note that these curves are, at least qualitatively, similar to the marginal stability curves corresponding to the two-layer QG model on an  $f$  plane with bottom slope. (The marginal stability diagram for the analogous  $\beta$ -plane problem appears in Fig. 7.11.3 in [Pedlosky 1987](#).) Since we have required that  $\alpha \ll 1$ , indeed, we would expect to recover the QG limit. The critical interfacial slopes and critical phase speeds as functions of the total wavenumber are given by, respectively,

$$\alpha_c = \frac{c}{K^2(2 - \mu K^2)}, \quad c = \frac{K^2(2 - \mu K^2)}{c}, \quad (6.15)$$

where  $\mu = 1$  on the upper branch,  $\mu = -1$  on the lower branch. [Equation \(6.10\)](#) also implies that  $B = \mu A$  on the MSC.

In order to determine the finite amplitude evolution of a marginally unstable mode, it is convenient to introduce

$$(p, h) = h_0(y) + s^2(p', h')(x, y, t, X, T) \quad (6.14)$$

into the nonlinear governing [equations \(2.1\)](#) and [\(2.2\)](#), where  $h_0$  is given in [\(6.2\)](#). The nonlinear interactions induce temporal and spatial variations on the order of  $t \cong O(s^{-1})$  and  $x \cong O(s^{-2})$ , respectively. Thus we introduce slow time and space scales,  $T = st$  and  $X = s^2x$ , so that

$$\partial_t \rightarrow \partial_t + s\partial_T, \quad \partial_x \rightarrow \partial_x + s^2\partial_X. \quad (6.15)$$

Finally, we impose a small supercriticality in the interfacial slope in the form,

$$\alpha = \alpha_c + \mu\delta^2s^2, \quad (6.16)$$

where  $\delta$  is an  $O(1)$  free parameter.

Substitution of [\(6.1\)](#), [\(6.3\)](#), [\(6.14\)](#), [\(6.15\)](#), and [\(6.16\)](#) into [\(2.1\)](#) and [\(2.2\)](#), dropping the primes, gives the nonlinear perturbation equations

$$\begin{aligned} & h_t + \alpha_c \Delta h_x + \alpha_c p_x \\ &= -s\alpha_c^2 h_{xy} - s\alpha_c^2 \left( y - \frac{L}{2} \right) \Delta h_x - sh_T \\ & \quad - sJ(\Delta h + p, h) - s^2\alpha_c \left( y - \frac{L}{2} \right) J(\Delta h, h) \\ & \quad - \mu\delta^2s^2(\Delta h + p)_x \\ & \quad - s^2\alpha_c [h\Delta h_x + 2h_y h_{xy} - h_x h_{yy} + h_x h_{xx}], \quad (6.17) \end{aligned}$$

$$\begin{aligned} & (\Delta p + h)_t + (\alpha_c - 1)p_x \\ &= -sJ(p, \Delta p + h) - s(\Delta p + h)_T - \mu\delta^2s^2 p_x. \quad (6.18) \end{aligned}$$

Both  $h$  and  $p$  are expanded in the small parameter  $s$ ,

$$(p, h)(x, y, t; X, T) = (p, h)^{(0)}(x, y, t; X, T) + s(p, h)^{(1)}(x, y, t; X, T) + \dots, \quad (6.19)$$

with the implicit requirement that  $p^{(0)}$ ,  $h^{(0)}$ ,  $p^{(1)}$ ,  $h^{(1)}$ , etc. are all  $O(1)$  quantities.

Next, we examine the  $O(1)$ ,  $O(s)$ , and  $O(s^2)$  problems, the details of which are contained in the appendix. The result is that the leading-order geostrophic pressures are given by [\(6.9\)](#), with  $B = \mu A$ , and the slow space–time evolution of  $A$  governed by the amplitude equation,

$$A_{TT} = \sigma A + iPA_X - NA(|A|^2 - |A_0|^2). \quad (6.20)$$

The coefficients  $\sigma$ ,  $P$ , and  $N$  are functions of  $k$ ,  $l$ ,  $\delta$ , and  $\mu$ , while  $A_0(X) = A(X, 0)$  is the initial perturbation amplitude profile. The expressions for the coefficients contain a large number of terms and in practice were evaluated using Maple.

If we neglect spatial dependence in the amplitude equation, then the solution for  $A$  will be determined by the signs of  $\sigma$  and  $N$ , and the value of  $A_0$ . In general,  $\sigma > 0$  implies linear instability,  $\sigma < 0$  implies linear stability,  $N > 0$  implies nonlinear stability, and  $N < 0$  implies nonlinear instability. We would expect that, given a marginally unstable mode, linear instability would cause exponential growth until the perturbation amplitude reached finite size, at which point the nonlinear term would suppress the growth. While the expressions for  $\sigma$  and  $N$  are prohibitively long to include here, it is interesting to point out that the nonlinear term can serve to stabilize as well as destabilize a linearly unstable flow. That is to say in the latter case,  $k$ ,  $l$ ,  $\delta$ , and  $\mu$  can be chosen in such a way that  $\sigma > 0$  and  $N < 0$ , leading to explosive growth. There exists evidence of weakly nonlinear modulation of the instability in some of our simulations. We believe, however, that it is the ‘‘explosive growth’’ that

allows a perturbation to quickly leave the weakly nonlinear regime and form large-scale structures such as meanders and eddies. Presumably, this rapid growth is halted by fully nonlinear interactions, for which no theory exists at this time.

A steadily travelling solitary wave is a possible solution to (6.20). Defining

$$\bar{\sigma}(X) \equiv -(\sigma + N|A_0|^2), \quad (6.21)$$

(6.20) can be rearranged to yield

$$A_{TT} + \bar{\sigma}A - iPA_X + NA|A|^2 = 0. \quad (6.22)$$

This is known as the unstable nonlinear Schrödinger (UNLS) equation (Yajima and Wadati 1990) and is a special case of the Ginzburg–Landau equation. It becomes the conventional nonlinear Schrödinger equation when  $T$  and  $X$  are interchanged (Tan and Liu 1995). Imposing the transformation,

$$A(X, T) = \exp\left(-\frac{i}{P} \int_0^X \bar{\sigma}(\xi) d\xi\right) C(X, T), \quad (6.23)$$

and simplifying allows us to recast (6.22) as the standard form of the UNLS equation,

$$C_{TT} - iPC_X + NC|C|^2 = 0. \quad (6.24)$$

The function  $C$  is assumed to be the product of a wave field dependent on  $X$  and  $T$  and an unknown function dependent on  $X - UT$  only, where  $U$  is the speed of the soliton. Having determined  $C$  (following Tan and Liu 1995), the solution  $A$  may be written as

$$A(X, T) = \sqrt{\frac{2}{N}} \eta \exp\left[i\left(\frac{\sigma}{P} + R\right)X + i\frac{2U\eta}{P} \tanh\left(\frac{\eta}{U}X\right) - i\frac{P}{2U}T\right] \operatorname{sech}\left[\frac{\eta}{U}(X - UT)\right], \quad (6.25)$$

where

$$R = \frac{S^2 - \eta^2}{P}, \quad S = \frac{P}{2U}, \quad (6.26)$$

while  $\eta$  and  $U$  are free parameters.

It is evident that, while the velocity of the envelope is amplitude independent, the velocity of the carrier wave is not. Figure 9 is a contour plot of the upper-layer thickness at  $t = 0$ , which consists of the wedge front plus the soliton envelope from (6.25). The wedgelike interface has a minimum of 0.5 and maximum of 1.5, while the soliton increases the maximum upper-layer thickness to 1.7. The contour interval is 0.1. For the purposes of illustration, we have neglected the internal wave structure of the soliton, as well as the  $x$  variation of the perturbation.

## 7. Conclusions

Numerical results of a series of simulations modeling buoyancy-driven surface currents have been presented. The algorithm consisted of the discretized Swaters (1993) model, which emphasizes the role of baroclinic instability, vortex-tube stretching, and a sloping bottom. Unlike many previous models, the SBFM does not rely on the two-layer QG approximation or the reduced gravity ansatz. One advantage of the model is that the interfacial outcropping is determined automatically, as a consequence of integrating the upper-layer equation. This is not true of shallow-water models in general.

Predicted length scales and phase speeds of growing instabilities on an isolated front are consistent with simulations of upwelling currents in previous studies. Growth rates are somewhat underestimated, probably due to the emphasis on baroclinicity in the model derivation. Our experiments demonstrate the development of meanders, filaments, and eddies, in agreement with primitive equation numerical models as well as observations off the western North American coast. Warm core eddies produced by pinching off of meanders are distinct entities defined by isopycnals that outcrop on the surface. The rapidity of frontal evolution could be correlated with the bottom slope in a way consistent with QG theory and observations of the Gulf Stream. Moreover, it now seems possible to obtain a robust three-dimensional description of mesoscale variability from a model that is still amenable to some analytical investigation.

While western boundary currents exhibit larger spatial scales than their coastal and estuarine cousins (and are almost

certainly influenced by variations in the Coriolis force), the dynamics of baroclinic instability, wave growth, and saturation are similar. Appropriately scaled, the SBFM gives results qualitatively similar to previous numerical studies, such as [Chassignet et al. \(1990\)](#) and [Bush et al. \(1995\)](#). Future research will include application of the SBFM to specific surface-intensified currents, such as the Gaspé current, using actual boundary and bottom topography data. Preliminary quantitative results as to timescales and length have proven encouraging. A clearer link between finite amplitude theory and numerical integration of the full equations also needs to be established.

### Acknowledgments

The authors thank Dr. Richard H. Karsten for many enjoyable hours discussing this research. Preparation of this manuscript was supported in part by a Research Grant awarded by the Natural Sciences and Engineering Research Council (NSERC) of Canada and by Science Subventions awarded by the Department of Fisheries and Oceans of Canada and the Atmospheric Environment Service of Canada to G.E.S. and by a NSERC Postgraduate Scholarship and a Graduate Teaching Assistantship awarded to M.K.R.

---

### REFERENCES

- Arakawa, A., 1966: Computational design for long-term numerical integration of the equations of fluid motion: Two-dimensional incompressible flow. Part 1. *J. Comput. Phys.*, **1**, 119–143.
- Asselin, R. A., 1972: Frequency filters for time integrations. *Mon. Wea. Rev.*, **100**, 487–490. [Find this article online](#)
- Barth, J. A., 1989a: Stability of a coastal upwelling front. 1. Model development and stability theorem. *J. Geophys. Res.*, **94**, 10 844–10 856.
- , 1989b: Stability of a coastal upwelling front. 2. Model results and comparison with observations. *J. Geophys. Res.*, **94**, 10 857–10 883.
- Benoit, J., M. I. El-Sabh, and C. L. Tang, 1985: Structure and seasonal characteristics of the Gaspé Current. *J. Geophys. Res.*, **90**, 3225–3236.
- Boss, E., N. Paldor, and L. Thompson, 1996: Stability of a potential vorticity front: From quasi-geostrophy to shallow water. *J. Fluid Mech.*, **315**, 65–84.
- Bush, A. B. G., J. C. McWilliams, and W. R. Peltier, 1995: The formation of oceanic eddies in symmetric and asymmetric jets. Part I: Early time evolution and bulk eddy transports. *J. Phys. Oceanogr.*, **25**, 1959–1979. [Find this article online](#)
- Charney, J. G., and G. R. Flierl, 1981: Oceanic analogues of large-scale atmospheric motion. *Evolution of Physical Oceanography—Scientific Surveys in Honor of Henry Stommel*, B. A. Warren and C. Wunsch, Eds., The MIT Press, 504–548.
- Chassignet, E. P., and B. Cushman-Roisin, 1991: On the influence of a lower layer on the propagation of nonlinear oceanic eddies. *J. Phys. Oceanogr.*, **21**, 939–957. [Find this article online](#)
- , D. B. Olson, and D. B. Boudra, 1990: Motion and evolution of oceanic rings in a numerical model and in observations. *J. Geophys. Res.*, **95**, 22 121–22 140.
- Cushman-Roisin, B., 1986: Frontal geostrophic dynamics. *J. Phys. Oceanogr.*, **16**, 117–127. [Find this article online](#)
- , and S. Merchant-Both, 1995: Elliptical warm core rings in a two-layer ocean with ambient shear. *J. Phys. Oceanogr.*, **25**, 2011–2024. [Find this article online](#)
- , G. G. Sutyryn, and B. Tang, 1992: Two-layer geostrophic dynamics. Part I: Governing equations. *J. Phys. Oceanogr.*, **22**, 132–143. [Find this article online](#)
- Gill, A. E., 1982: *Atmosphere–Ocean Dynamics*. Academic Press, 662 pp.
- Griffiths, R. W., and P. F. Linden, 1981: The stability of buoyancy-driven coastal currents. *Dyn. Atmos. Oceans*, **5**, 281–306.
- , and —, 1982: Laboratory experiments on fronts. Part 1: Density-driven boundary currents. *Geophys. Astrophys. Fluid Dyn.*, **19**, 159–187.
- , P. D. Killworth, and M. E. Stern, 1982: Ageostrophic instability of ocean currents. *J. Fluid Mech.*, **117**, 343–377.
- Haidvogel, D. B., A. Beckmann, and K. S. Hedström, 1991: Dynamical simulations of filament formation and evolution in the coastal transition zone. *J. Geophys. Res.*, **96**, 15 017–15 040.
- Holland, W. R., and D. B. Haidvogel, 1980: A parameter study of the mixed instability of idealized ocean currents. *Dyn. Atmos. Oceans*, **4**, 185–215.
- Ikeda, M., and W. J. Emery, 1984: Satellite observations and modeling of meanders in the California current system off Oregon and Northern California. *J. Phys. Oceanogr.*, **14**, 1434–1450. [Find this article online](#)

- ,— ,— and L. A. Mysak, 1984: Seasonal variability in meanders of the California Current System off Vancouver Island. *J. Geophys. Res.*, **89**, 3487–3505..
- Karsten, R. H., and G. E. Swaters, 1996: A note on the stability theory of buoyancy-driven ocean currents over a sloping bottom. *Z. Angew Math. Phys.*, **47**, 28–38..
- Killworth, P. D., 1983: Long wave instability of an isolated front. *Geophys. Astrophys. Fluid Dyn.*, **25**, 235–258..
- ,— and M. E. Stern, 1982: Instabilities on density-driven boundary currents and fronts. *Geophys. Astrophys. Fluid Dyn.*, **22**, 1–28..
- ,— N. Paldor, and M. E. Stern, 1984: Wave propagation and growth on a surface front in a two-layer geostrophic current. *J. Mar. Res.*, **42**, 761–785..
- Kosro, P. M., 1987: Structure of the coastal current field off northern California during the Coastal Ocean Dynamics Experiment. *J. Geophys. Res.*, **92**, 1637–1654..
- McCreary, J. P., Y. Fukamachi, and P. K. Kundu, 1991: A numerical investigation of jets and eddies near an eastern ocean boundary. *J. Geophys. Res.*, **96**, 2515–2534..
- Mechoso, C. R., and D. M. Sinton, 1981: Instability of baroclinic flows with horizontal shear along topography. *J. Phys. Oceanogr.*, **11**, 813–821.. [Find this article online](#)
- Mertz, G., M. I. El-Sabh, D. Proulx, and A. R. Condal, 1988: Instability of a buoyancy-driven coastal jet: The Gaspé Current and its St. Lawrence precursor. *J. Geophys. Res.*, **93**, 6885–6893..
- ,— Y. Gratton, and J. A. Gagné, 1990: Properties of unstable waves in the St. Lawrence Estuary. *Atmos.–Ocean*, **28**, 230–240..
- Paldor, H., 1983: Stability and stable modes of coastal fronts. *Geophys. Astrophys. Fluid Dyn.*, **27**, 217–228..
- ,— and P. D. Killworth, 1987: Instabilities of a two-layer coupled front. *Deep-Sea Res.*, **34**, 1525–1539..
- ,— and M. Ghil, 1990: Finite wavelength instabilities of a coupled density front. *J. Phys. Oceanogr.*, **20**, 114–123.. [Find this article online](#)
- Pavía, E. G., 1992: The breakup of frontal filaments. *J. Phys. Oceanogr.*, **22**, 399–403.. [Find this article online](#)
- Pedlosky, J., 1970: Finite-amplitude baroclinic waves. *J. Atmos. Sci.*, **27**, 15–30.. [Find this article online](#)
- ,— 1972: Finite-amplitude baroclinic wave packets. *J. Atmos. Sci.*, **29**, 680–686.. [Find this article online](#)
- ,— 1982: Finite-amplitude baroclinic waves at minimum critical shear. *J. Atmos. Sci.*, **39**, 555–562.. [Find this article online](#)
- ,— 1983: The growth and decay of finite-amplitude baroclinic waves. *J. Atmos. Sci.*, **40**, 1863–1876.. [Find this article online](#)
- ,— 1987: *Geophysical Fluid Dynamics*. 2d ed. Springer-Verlag, 710 pp..
- Phillips, N. A., 1954: Energy transformations and meridional circulations associated with simple baroclinic waves in a two level quasi-geostrophic model. *Tellus*, **6**, 273–286..
- Reszka, M. K., 1997: Finite amplitude waves and eddy formation on a baroclinically unstable front over a sloping bottom. M.S. thesis, Department of Mathematical Sciences, University of Alberta, 189 pp. [Available from Dr. Gordon E. Swaters, Dept. of Mathematical Sciences, University of Alberta, 632 Central Academic Building, Edmonton, AB T6G 2G1, Canada.]
- Robinson, A. R., Ed., 1983: *Eddies in Marine Science*. Springer-Verlag, 609 pp..
- Samelson, R. M., and D. C. Chapman, 1995: Evolution of the instability of a mixed-layer front. *J. Geophys. Res.*, **100**, 6743–6759..
- Swaters, G. E., 1993: On the baroclinic dynamics, Hamiltonian formulation, and general stability characteristics of density-driven surface currents and fronts over a sloping continental shelf. *Philos. Trans. Roy. Soc. London*, **345A**, 295–325..
- Tan, B., and S. Liu, 1995: Collision interactions of solitons in a baroclinic atmosphere. *J. Atmos. Sci.*, **52**, 1501–1512.. [Find this article online](#)
- Yajima, T., and M. Wadati, 1990: Soliton solution and its property of unstable nonlinear Schrödinger equation. *J. Phys. Soc. Japan*, **59**, 41–47..
- Zwillinger, D., 1989: *Handbook of Differential Equations*. Academic Press, 787 pp..

---

## APPENDIX

### 8. Details of the Weakly Nonlinear Calculation

#### a. $O(1)$ problem

The  $O(1)$  problem is

$$h_t^{(0)} + \alpha_c \Delta h_x^{(0)} + \alpha_c p_x^{(0)} = 0, \quad (\text{A.1})$$

$$(\Delta p^{(0)} + h^{(0)})_t + (\alpha_c - 1)p_x^{(0)} = 0 \quad (\text{A.2})$$

with the boundary condition

$$(p, h)^{(0)}_x = 0 \quad (\text{A.3})$$

at  $y = 0, L$ . The normal-mode solutions are

$$(p, h)^{(0)} = (A, B)(X, T) \exp[ik\theta] \sin(ly) + \text{c.c.}, \quad (\text{A.4})$$

where  $\theta = x - ct$  is the phase and  $B = \mu A$ .

### b. $O(s)$ problem

The  $O(s)$  problem is linear, and is given by

$$h_t^{(1)} + \alpha_c \Delta h_x^{(1)} + \alpha_c p_x^{(1)} = -\alpha_c^2 \left( y - \frac{L}{2} \right) \Delta h_x^{(0)} - \alpha_c^2 h_{xy}^{(0)} - h_T^{(0)}, \quad (\text{A.5})$$

$$(\Delta p^{(1)} + h^{(1)})_t + (\alpha_c - 1)p_x^{(1)} = -(\Delta p^{(0)} + h^{(0)})_T. \quad (\text{A.6})$$

The solutions are of the form ([Reszka 1997](#)),

$$(p, h)^{(1)} = (\bar{p}, \bar{h})(y, X, T) \exp[ik\theta] + \text{c.c.} + (\Psi, \Phi)(y, X, T), \quad (\text{A.7})$$

where we have introduced the mean-flow correction terms  $\Psi$  and  $\Phi$ . These are needed to account for changes to the mean flow caused by interaction of nonlinear terms, as will be evident in the  $O(s^2)$  problem ([Pedlosky 1987](#)).

Substituting [\(A.7\)](#) into [\(A.5\)](#) and [\(A.6\)](#), and dividing through by  $i\alpha_c k$  and  $-ick$ , respectively, we obtain

$$\left[ \partial_{yy} - k^2 - \frac{c}{\alpha_c} \right] h + \bar{p} = -\alpha_c \mu A \cos(ly) + \alpha_c \left( y - \frac{L}{2} \right) K^2 \mu A \sin(ly) + \frac{i\mu}{\alpha_c k} A_T \sin(ly), \quad (\text{A.8})$$

$$\left[ \partial_{yy} - k^2 - \frac{\alpha_c - 1}{c} \right] \bar{p} + h = \frac{i}{kc} (K^2 A - \mu A)_T \sin(ly). \quad (\text{A.9})$$

*(Click the equation graphic to enlarge/reduce size)*

Since the associated homogenous problem is self-adjoint, it follows, by the Fredholm alternative theorem (e.g., [Zwillinger 1989](#)), that the inhomogeneous problem [\(A.8\)](#) and [\(A.9\)](#) has solutions if, and only if,

$$\int_0^L \left[ -\alpha_c \mu A \cos(ly) + \alpha_c K^2 \left( y - \frac{L}{2} \right) \mu A \sin(ly) + \frac{i\mu}{\alpha_c k} A_T \sin(ly) \right] \mu A \sin(ly) dy$$

$$+ \int_0^L \left[ \frac{i}{kc} (K^2 A - \mu A)_T \sin(ly) \right] A \sin(ly) dy = 0. \quad (\text{A.10})$$

*(Click the equation graphic to enlarge/reduce size)*

The left-hand side may be written as

$$-\alpha_c \mu A^2 \int_0^L \sin(ly) \cos(ly) dy + \alpha_c K^2 A^2 \int_0^L \left( y - \frac{L}{2} \right) \sin^2(ly) dy + \frac{i}{k} \left( \frac{1}{\alpha_c} + \frac{K^2 - \mu}{c} \right) A A_T \int_0^L \sin^2(ly) dy.$$

*(Click the equation graphic to enlarge/reduce size)*

Each of the first two terms integrates to zero. The last term also vanishes when the expressions in [\(6.13\)](#) are substituted for  $\alpha_c$  and  $c$ . Therefore the integral in [\(A.10\)](#) trivially vanishes, so the  $O(s)$  problem is degenerate in the sense that it gives us no new condition on  $A$ .

To examine the next order problem, we have to determine the solutions  $\tilde{h}, \tilde{P}$  subject to the no-normal-flow condition on the channel walls. The derivation splits into two cases depending on the sign of  $l^2 - 2\mu$ . After a little algebra, it can be shown that, for the case where  $l^2 - 2\mu > 0$ , the  $O(s)$  tilde solutions are

$$\tilde{p}(y, T) = \gamma_1 \left(y - \frac{L}{2}\right)^2 \cos(ly) + \gamma_2 \left(y - \frac{L}{2}\right) \sin(ly) + \gamma_3 \cos(ly) + \gamma_4 \sin(ry) + \gamma_5 \sin[r(y - L)], \quad (\text{A.11})$$

$$h(y, T) = -[\partial_{yy} + l^2 - \mu]\tilde{p} + \frac{i}{kc}(K^2 - \mu) \sin(ly)A_T, \quad (\text{A.12})$$

(Click the equation graphic to enlarge/reduce size)

with

$$\left. \begin{aligned} \gamma_1 &= -\frac{K^2}{8l}\alpha_c A, & \gamma_2 &= \left[ \frac{\mu K^2 - 1}{4} + \frac{1}{2} \left(\frac{K}{2l}\right)^2 \right] \alpha_c A, & \gamma_3 &= \left[ \frac{K^2 L^2}{32l} + \frac{l(K^2 - \mu)}{4} \right] \alpha_c A, \\ \gamma_4 &= \frac{l(K^2 - \mu)(-1)^{n+1}}{4 \sin(rL)} \alpha_c A, & \gamma_5 &= \frac{l(K^2 - \mu)}{4 \sin(rL)} \alpha_c A, & r &= \sqrt{l^2 - 2\mu} \end{aligned} \right\}. \quad (\text{A.13})$$

(Click the equation graphic to enlarge/reduce size)

The case  $l^2 - 2\mu < 0$  can only occur if  $\mu > 0$  (i.e.,  $\mu = 1$ ). Then, without loss of generality, we set  $\mu = 1$ , and the  $O(s)$  tilde solutions are

$$\tilde{p}(y, T) = \gamma_1 \left(y - \frac{L}{2}\right)^2 \cos(ly) + \gamma_2 \left(y - \frac{L}{2}\right) \sin(ly) + \gamma_3 \cos(ly) + \bar{\gamma}_4 \exp(-\bar{r}y) + \bar{\gamma}_5 \exp[\bar{r}(y - L)], \quad (\text{A.14})$$

$$h(y, T) = -[\partial_{yy} + l^2 - 1]\tilde{p} + \frac{i}{kc}(K^2 - 1) \sin(ly)A_T \quad (\text{A.15})$$

(Click the equation graphic to enlarge/reduce size)

with  $\gamma_1, \gamma_2$ , and  $\gamma_3$  as above and

$$\left. \begin{aligned} \bar{\gamma}_4 &= \frac{((-1)^n \exp(-\bar{r}L) - 1)(K^2 - 1)l}{4(1 - \exp(-2\bar{r}L))} \alpha_c A, \\ \bar{\gamma}_5 &= \frac{(\exp(-\bar{r}L) - (-1)^n)(K^2 - 1)l}{4(1 - \exp(-2\bar{r}L))} \alpha_c A, & \bar{r} &= \sqrt{2 - l^2} \end{aligned} \right\}. \quad (\text{A.16})$$

### c. $O(s^2)$ problem

The  $O(s^2)$  problem is given by

$$\begin{aligned} h_r^{(2)} + \alpha_c \Delta h_x^{(2)} + \alpha_c p_x^{(2)} &= -\alpha_c^2 \left(y - \frac{L}{2}\right) \Delta h_x^{(1)} - \alpha_c^2 h_{xy}^{(1)} - h_y^{(0)} \Delta h_x^{(1)} - h_y^{(1)} \Delta h_x^{(0)} + h_x^{(0)} \Delta h_y^{(1)} + h_x^{(1)} \Delta h_y^{(0)} \\ &\quad - J(p^{(0)}, h^{(1)}) - J(p^{(1)}, h^{(0)}) - h_r^{(1)} - \mu \delta^2 \Delta h_x^{(0)} - \mu \delta^2 p \\ &\quad - \alpha_c [h^{(0)} \Delta h_x^{(0)} + 2h_y^{(0)} h_{xy}^{(0)} - h_x^{(0)} h_{yy}^{(0)} + h_x^{(0)} h^{(0)} h_{xx}^{(0)}] + h_r^{(0)} \\ &\quad - \alpha_c \Delta h_x^{(0)} - 2\alpha_c h_{xxx}^{(0)} - \alpha_c p_{xx}^{(0)}, \end{aligned} \quad (\text{A.17})$$

(Click the equation graphic to enlarge/reduce size)

$$\begin{aligned} (\Delta p^{(2)} + h^{(2)})_t + (\alpha_c - 1)p_x^{(2)} &= -(\Delta p^{(1)} + h^{(1)})_T - 2p_{xx}^{(0)} - (\Delta p^{(0)} + h^{(0)})_T - (\alpha_c - 1)p_x^{(0)} \\ &\quad - J(p^{(0)}, \Delta p^{(1)} + h^{(1)}) - J(p^{(1)}, \Delta p^{(0)} + h^{(0)}) - \mu \delta^2 p_x^{(0)}. \end{aligned} \quad (\text{A.18})$$

(Click the equation graphic to enlarge/reduce size)

Terms on the right-hand side of (A.17) and (A.18) without fast-phase oscillation lead to particular solutions that will grow linearly in  $t$ , so to avoid this secular growth the sum of these terms must be set equal to zero. Employing the identity  $AA^*_T + A^*A_T = (|A|^2)_T$ , we obtain

$$\Psi_T + 2\frac{l}{c}(K^2 - \mu) \sin(ly) \cos(ly)(|A|^2)_T = 0, \quad (\text{A.19})$$

$$\Psi_{yyT} + \Phi_T + 2\frac{l}{c}(K^2 - \mu) \sin(ly) \cos(ly)(|A|^2)_T = 0. \quad (\text{A.20})$$

Imposing the conditions

$$\Psi = 0 \quad \text{at } t = 0, \quad (\text{A.21})$$

$$\Psi_{yT} = 0 \quad \text{on } y = 0, L, \quad (\text{A.22})$$

it follows that

$$\Phi(y; X, T) = -\frac{l}{c}(K^2 - \mu) \sin(2ly)(|A|^2 - |A_0|^2), \quad (\text{A.23})$$

$$\Psi \equiv 0, \quad (\text{A.24})$$

where  $A_0(X) = A(X, T = 0)$ .

Upon substituting  $\Phi$  and  $\Psi$  into the  $O(s^2)$  problem, we consider all the terms associated with  $\exp(\pm ik\theta)$ . According to the Fredholm alternative theorem, solutions of the form

$$(p, h)^{(2)} = (\hat{p}, \hat{h})(y; X, T) \exp[ik\theta] + \text{c.c.} \quad (\text{A.25})$$

exist if and only if

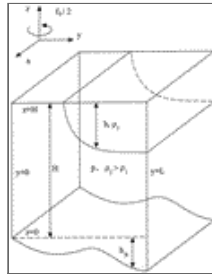
$$\int_0^L \left\{ \mu \alpha_c k^2 \left( y - \frac{L}{2} \right) h - \mu \alpha_c h_y - \mu \alpha_c \left( y - \frac{L}{2} \right) h_{yy} + \mu \frac{i}{k \alpha_c} h_T + \mu \frac{\delta^2}{\alpha_c} (K^2 - \mu) \sin(ly) A + \frac{ik}{c} \tilde{p}_T - \frac{i}{kc} \tilde{p}_{yyT} \right. \\ \left. - \frac{i}{kc} h_T + \mu \frac{\delta^2}{c} \sin(ly) A - 2l^2 K^4 \frac{(K^2 - 2\mu)^2}{K^2 - \mu} [4l^2 (K^2 - \mu) - K^2 (K^2 - 2\mu)] \right. \\ \left. \times \sin(ly) \cos(2ly) A (|A|^2 - |A_0|^2) \right\} \sin(ly) A \, dy = 0. \quad (\text{A.26})$$

*(Click the equation graphic to enlarge/reduce size)*

Substituting in (6.13), (A.11) and (A.12), [or (A.14) and (A.15) as appropriate], we integrate in  $y$ , divide through by the coefficient of  $A_{TT}$  and rearrange to obtain the amplitude equation,

$$A_{TT} = \sigma A + iPA_X - NA(|A|^2 - |A_0|^2). \quad (\text{A.27})$$

## Figures



[Click on thumbnail for full-sized image.](#)

Fig. 1. Model geometry associated with (2.1) and (2.2) (symbols defined in text). The model derivation assumes a rigid lid. While general bottom topography is allowed, our simulations employ an  $x$ -invariant bottom.

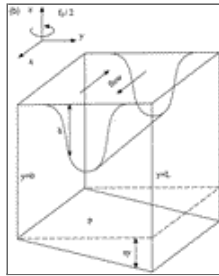






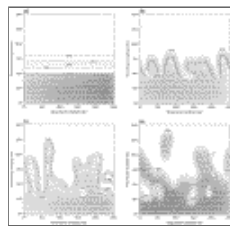
[Click on thumbnail for full-sized image.](#)

Fig. 2a. Model geometry where the fluid interface forms an isolated front. This frontal profile was used in our jet simulations.



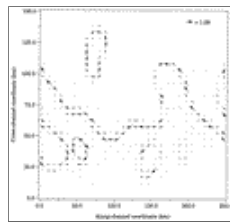
[Click on thumbnail for full-sized image.](#)

Fig. 2b. Model geometry where the fluid interface forms a coupled front. This frontal profile was used in our shear flow simulations.



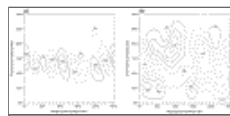
[Click on thumbnail for full-sized image.](#)

Fig. 3. Upper-layer thickness at (a) day 0, (b) day 9, (c) day 15, and (d) day 18 for an isolated front simulation. Contour values range from 0 to 50 m and the contour intervals are 12.5 m for all four plots. Regions where  $h = 0$  are shaded. In (a) the front is uniform in  $x$  (only the lower-layer pressure is perturbed). In (b) disturbances with an along-channel wavelength of 63 km have developed. Wavebreaking is also present. In (c) a warm core eddy and several fingerlike growths can be observed. In (d) there are three isolated eddies (two warm core and one cold core). Another warm core eddy is about to detach.



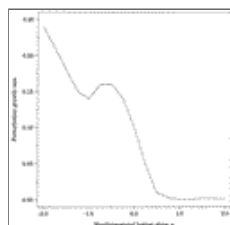
[Click on thumbnail for full-sized image.](#)

Fig. 4. Geostrophic velocity field for the upper layer at day 18. The current has intensified and local velocities of  $0.8\text{--}1.0\text{ m s}^{-1}$  occur throughout.



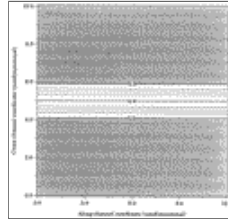
[Click on thumbnail for full-sized image.](#)

Fig. 5. Nondimensional lower-layer pressure at (a) day 9 and (b) day 18 (i.e., corresponding to [Figs. 3b,d](#), respectively). In (a) the random perturbation has organized itself into a wave train localized beneath the front. Contour values range from  $-0.5$  to  $0.3$  with an interval of  $0.2$ . In (b) the  $p$  field has evolved into a collection of high and low pressure cells in response to meanders and eddies present in the upper layer. Contour values range from  $-1.8$  to  $1.4$  with an interval of  $0.4$ .



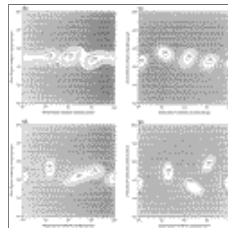
[Click on thumbnail for full-sized image.](#)

Fig. 6. Lower-layer KE (nondimensional) versus bottom slope,  $s$ , for a series of isolated front simulations. In our tests, the values of  $s$  most conducive to eddy formation were negative (i.e., a negative slope whose slope is anticorrelated with the average slope of the interface).



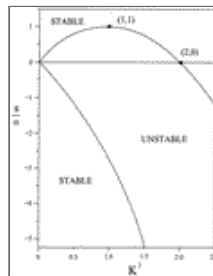
[Click on thumbnail for full-sized image.](#)

Fig. 7. Upper-layer thickness at nondimensional times (a)  $t = 0$ , (b)  $t = 3$ , (c)  $t = 5$ , (d)  $t = 8$ , and (e)  $t = 13$  for a coupled front simulation. Contour values range from 0 to 0.8 with a contour interval of 0.2. The shear flow current (a) promptly breaks up (b) into distinct warm-core eddies (c). Plot (d) shows a merger of two eddies. In plot (e) the merged eddy has split apart again.



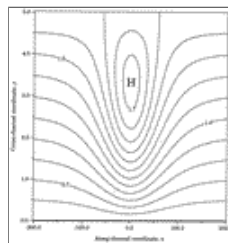
[Click on thumbnail for full-sized image.](#)

Fig. 7. (Continued)



[Click on thumbnail for full-sized image.](#)

Fig. 8. Marginal stability curves (MSC) for a gently sloping wedge front, relating the bottom slope  $s$ , the interface slope  $\alpha$ , and the total wavenumber  $K$ . Linear analysis predicts stability with respect to perturbations everywhere between the two curves of the MSC.



[Click on thumbnail for full-sized image.](#)

Fig. 9. Contour plot of the total upper-layer thickness, consisting of the wedge profile plus the soliton envelope obtained from our weakly nonlinear analysis [see (5.49)]. The contours range between 0.5 and 1.7, with a contour interval of 0.1. This plot corresponds to  $t = 0$ ,  $s = \alpha_c = 0.2$ ,  $\sigma = 0.8$ ,  $N = 0.4$ ,  $P = \eta = -0.3$ ,  $U = 0.5$ . The  $x$  variation of the perturbation as well as the internal oscillatory structure of the soliton have been eliminated.

Dedicated to the memory of Gordon Mertz.

Corresponding author address: Dr. Gordon E. Swaters, Department of Mathematical Sciences, University of Alberta, 632 Central Academic Building, Edmonton, AB T6G 2G1, Canada.

E-mail: [gordon.swaters@ualberta.ca](mailto:gordon.swaters@ualberta.ca)



© 2008 American Meteorological Society [Privacy Policy and Disclaimer](#)  
Headquarters: 45 Beacon Street Boston, MA 02108-3693  
DC Office: 1120 G Street, NW, Suite 800 Washington DC, 20005-3826  
[amsinfo@ametsoc.org](mailto:amsinfo@ametsoc.org) Phone: 617-227-2425 Fax: 617-742-8718  
[Allen Press, Inc.](#) assists in the online publication of *AMS* journals.